Interplanetary consequences and geoeffectiveness of CME associated with major solar flare from NOAA AR 12673

Shirsh Lata Soni[1], Radhe Shyam Gupta[1] and Pyare Lala Verma[2]

[1] Department of Physics, Govt. P.G. College, Satna, MP 485001, India; *sheersh171@gmail.com*
[2] Department of Physics, Govt. P.G. College Maihar, Satna, MP, India

Abstract In this reported work, we study a major X-class flare (X9.3) that arose from NOAA Active Region (AR) 12673 on 2017 September 6, from 11:53 UT to 12:10 UT in multi-wavelength views. This event also produced a fast coronal mass ejection (CME). NOAA AR 12673 emerged at S09W30 on 2017 September 6 and grew rapidly to a large AR. On 2017 September 9, the maximum area of this AR was 1060 millionth of the solar hemisphere. The group of sunspots disappeared over the west limb of the Sun (S09W83) on September 10. It was a fast emerging flux region. The group of sunspots showed magnetic configuration category alpha-beta-gamma. We identified their earliest signatures of eruption in AIA 94 Å images with initialization and successive rapid growth from low coronal heights of hot channeled structures. On the other hand, the CME associated with this flare event triggered the intense Dst at 1 AU (–142 nT). We have acquired observations and analyze the reported event from the Sun's surface, corona (source AR), interplanetary space and in-situ measurement near Earth. In addition, here we analyze the complex processes of CME-CME interaction that have contributed a significant role to make the reported event so geoeffective.

Key words: Solar wind — Coronal Mass Ejection (CME) — Sun

1 INTRODUCTION

One example of an extreme form of solar activity is known as the coronal mass ejections (CMEs), which is associated with eruptions of plasma and magnetic field at large-scale. It erupts from the Sun and moves into the interplanetary (IP) medium. When CMEs propagate into the IP medium, usually they are named interplanetary coronal mass ejections (ICMEs). A typical CME propagates into IP space at the velocity of 200–4000 km s^{-1}, and therefore possesses kinematic energy exceeding 10^{25} J and even carries a mass of 10^{12} kg. Its kinematics in IP space depend upon the initial (linear) speed of the CME and ambient solar wind conditions. Further, the propagation of CMEs keeps changing continually in between the Sun-Earth distance due to interaction with other CMEs. CMEs are accelerated and decelerated, but near Earth they come to a constant speed nearly equal to the speed of ambient solar wind (Manoharan 2006; Gopalswamy et al. 2001a, 2005; Gosling et al. 1973; Richardson & Cane 2010). Large scale changes in the configuration of the coronal magnetic field are produced by CMEs associated with solar eruptive flares. Earth directed CMEs are known as halo CMEs;

their plasma and magnetic structure have been regularly recorded by in-situ observations at 1 AU. These CMEs are known as drivers of hazardous effects in the near Earth environment. Geoeffectiveness is quantified by disturbance storm time (Dst) index. From in-situ observations, we can examine the geomagnetic activity and possible IP drivers for a geomagnetic storm (Lugaz et al. 2012; Shen et al. 2017). In early September 2017, NOAA Active Region (AR) 12673 passed through the visible disk of the Sun. This AR was extremely energetic and produced more than 80 flares including four X-class flares during an interval of 7 d (Shen et al. 2018). Two of these four flares, the major X-class flares (X9.3 and X8.2 flares), were the top two ranked flares of solar cycle 24 (Yan et al. 2018a,b). During the same period (2017 Sep 4–10), NOAA AR 12673 also produced about 20 CMEs and these CMEs could have interacted with each other (in IP space) during their propagation inside the Sun-Earth distance. In addition, near Earth observations measured an intense geomagnetic storm (Dst –142 nT) on 2017 September 8, at 02:00 UT. Thus, we can expect that this intense geomagnetic disturbance was due to these CMEs. Many researchers, i.e., Mitra et al. (2018); Inoue et al. (2018); Jiang et al. (2018) investigated

this major event that occurred on Sep 2017. They reported results from the associated magnetohydrodynamic simulation, magnetic complexity and features of the AR during the pre-flare phase, flare eruption and study near Sun observations, while in this present work we have examined the IP conditions and geoeffectiveness along with photospheric features from the CME associated with the X-class flare event from 2017 Sep 6. In this work, we consider the radial evolution and propagation of CMEs associated with the largest flare in the current solar cycle (solar cycle 24) which occurred on 2017 September 6. The flare erupted from NOAA AR 12673 located at S09W30 on the solar disk from 11:53 UT to 12:10 UT and reached its peak at time 12:02 UT. This CME occurred with the eruption of a major solar flare, of *Geostationary Operational Environmental Satellite* (*GOES*) class X9.3. At that time, it is the most interesting aspect of the solar region. To characterize the various phases of the CME from the solar surface to 1 AU, we used multi-instrumental, multi-wavelength and multi-point observations of the Sun and IP space. Here we observe a shock embedded in the ICME where a shock driven by a following ICME propagated into the ejecta region of the proceeding ICME (Shen et al. 2017) and the IP shock associated with this eruption from the Sun leads to the intense geomagnetic storm ($\mathrm{Dst} = -142\,\mathrm{nT}$) recorded at 02:00 UT on 2017 September 8.

2 DATA COLLECTION

In this work, we investigate multi-wavelength imaging of the largest flare followed by the CME event of one particular AR, NOAA AR 12673, and its IP consequences for solar cycle 24. The various data from different observatories will be considered for the analysis. Data from the Atmospheric Imaging Assembly (AIA) onboard the Solar Dynamics Observatory (SDO) are utilized for investigating the source region of the solar flare/CME. For the present study, we obtained and investigated extreme ultraviolet (EUV) images of the Sun recorded by AIA, 94 Å filter. The 94 Å filter is sensitive to plasma at extreme temperature (approximately 6 million K). A photospheric view of the active source region for each CME and flare event has been provided by the white light and magnetogram images from the Helioseismic and Magnetic Imager (HMI). White-light images observed by the Large Angle and Spectrometric COronagraph (LASCO) onboard the *Solar and Heliospheric Observatory* (*SOHO*) space mission provide the onset time and linear initial speed of CMEs. Details about these CMEs and their associated geomagnetic storm are taken from the online catalogs `http://cdaweb.gsfc.nasa.gov/istppub-lic/`, `http://wdc.kugi.kyoto.u.ac.jp/dstrealtime/index.html` and

`www.lesia.obspm.fr/cesra/highlights/highlight07-html/`. To investigate the initiation and evolution of the AR, we consider the category of its magnetic configuration and size. Detailed information on the magnetic configuration and area occupied by AR was collected from `ftp://ftp.swpc.noaa.gov/pub/warehouse/`. The arrival time of the CME is estimated from the time duration between the launch of a CME (as seen in LASCO images) and the time IP shock commenced at 1 AU. The geomagnetic storm commencement time is considered the time when the value of Dst (SYM/H) index start decreasing. The data on ICMEs and IP shocks, and which are listed in the Operating Missions as a Node on the Internet (OMNI) database, were obtained from in-situ observations of Advanced Composition Explorer (ACE)/Wind.

2.1 Prior Evolution and Initiation of CME/Flare

2.1.1 Multi-wavelength analysis of source region

The First appearance of source NOAA AR 12673 on the solar disk at the heliospheric location S08E62, with a simple magnetic configuration as beta type on 2017 Aug 30. The AR rose rapidly in terms of size and magnetic configuration as well. The source region turned into magnetic configuration alpha-beta-gamma type on 2017 Sep 5. The heliospheric and solar activities presented in this paper correspond to the major eruptive activity in NOAA AR 12673 on 2017 September 6 when the location of source AR was S09W30, near the solar disk center. As we can see from Figure 1, multi-wavelength imaging of the AR indicates the duration of selected activity. HMI/AIA intensity images clearly indicate the leading and following group of sunspots. The following group of sunspots is a complex mixed polarity region. To investigate the chromospheric and coronal structure, we present the AIA 94 Å images of the source region in panel (c) of Figure 1. From Figure 1(c), we can clearly verify the presence of a long S shaped filament channel (i.e., sigmoid) which extends over different parts of the AR. Several recent studies found that sigmoidal ARs are more prone to undergo more eruptions than non-sigmodal ARs (Canfield et al. 1999; Glover et al. 2000). The HMI continuum intensity and magnetogram images (Panels (a), (d) and (b), (e)) display the sunspot distribution and magnetic polarities, respectively. NOAA AR 12673 was the most active during 2017 September 6 to 2017 September 10. During this period, four X class flares (X9.3, X2.2, X1.3 and X8.2) along with 27 M class flares erupted (Yang et al. 2017). On 2017 September 6, NOAA AR 12673 underwent the most significant eruptive and flaring activity of solar cycle 24. In Figure 2, we indicate the evolution of the flare and its X-ray flux observed by
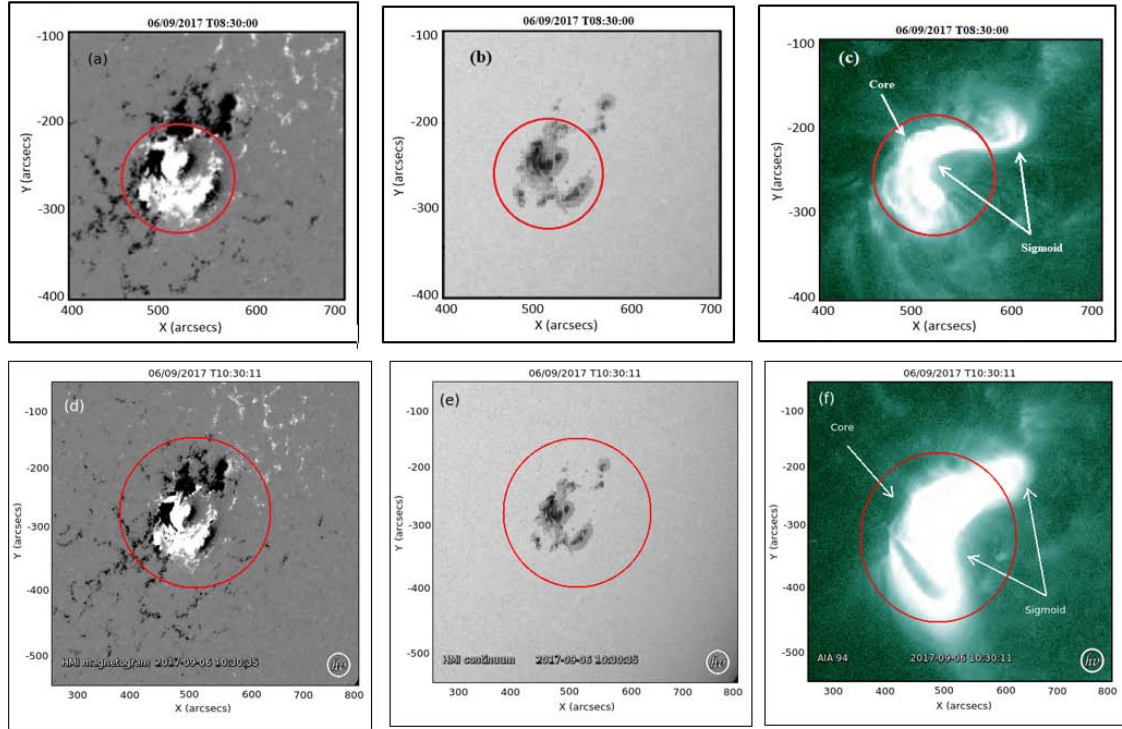
Fig. 1 Multiwavelength view on NOAA AR 12673 showing circumstance signatures of eruptive flares on 09:10 UT and 12:02 UT. Plots (a), (b) and (c) are the pre-AR images that manifest signatures of the flare (class X2.2) that occurred at 09:10 UT. In addition, plots (d), (e) and (f) display the the pre-flare eruptive signatures for a major flare event, class X9.3, at 12:02 UT. Plots (a), (d), and (b), (e): HMI continuum image (*white light*) and magnetogram of the source AR respectively. Plots (a), (d), and (b), (e) featuring distribution of sunspots and magnetic polarity respectively. In HMI magnetogram, in the photosphere, *white* indicates positive and *black* signifies negative magnetic polarity region. Plots (c) and (f): SDO/AIA image in the 94 Å wavelength range band indicating hot coronal loops which are twisted and form an S-shaped structure (sigmoid), marked as *arrows* in plots (c) and (f).
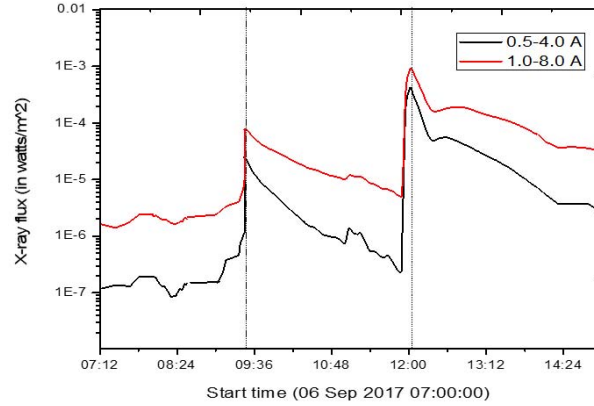
Fig. 2 Light curves indicating the evolution of eruptive flares observed by *GOES*. *Red line* indicates the X-ray flux in the 1.0–8.0 Å wavelength band and *black line* signifies the X-ray flux in the 0.5–4.0 Å wavelength band. *Vertical black dotted lines* at 09:00 UT and 12:02 UT mark peak phases of X2.2 and X9.3 flares respectively.

GOES at 12:02 UT on 2017 September 6. From the *GOES* curve, we observe that the flux started to build up from 08:57 UT onward and first peaked at 09:10 UT, which was an X2.2 class flare, then decayed afterward. After reaching a minimum at 09:20 UT, the X-ray flux further increased and manifested the second peak at 12:02 UT, which cor-

responded to an X9.3 flare. Both flares occurred at the location S09W30 from the same AR, NOAA AR 12673. The two flares are associated with a fast halo and a slow partial halo CMEs, respectively. AIA 94 Å image investigation during the pre-flare intervening time, displayed in Figure 1(c), shows the active region is enveloped by

twisted hot coronal loops that assume an S shaped structure (sigmoid), as predicted by theory. After the eruption of an X2.2 flare at 09:10, from Figure 1(f) we can see again see a semi-circular (S-shaped sigmoid) shape is present due to coronal loops. Amari et al. (2000) proposed a model for CMEs and flares, in which these twisted flux ropes, tracing the magnetic structures of filaments, play an important role (Amari et al. 2000). Eruption of the flux ropes stretched the overlying loops and, between the counter-directed lines below, re-connection takes place, resulting in eruption of solar flares (Joshi et al. 2018; Shibata 1999; Lin & Forbes 2000).

2.2 LASCO Observations

LASCO onboard *SOHO* images the Sun's corona from $2\,R_\odot$ to $30\,R_\odot$ in white light. LASCO consists of three coronagraph imaging instruments; first is a Fabry-Pérot interferometer coronagraph) imaging from 1.1 to $3\,R_\odot$ named C1, second is a white light coronagraph (C2) imaging from 1.5 to $6\,R_\odot$ (orange) and the third one is a coronagraph for white light imaging from 3.7 to $30\,R_\odot$ (blue) named C3, which operates by artificial occultation (Brueckner et al. 1995). From the LASCO catalog of CMEs (Gopalswamy et al. 2009), the eruption of a filament gives rise to a halo CME as shown in Figure 3. The first appearance of a CME was detected by the LASCO C2 coronagraph at a height of $3.93\,R_\odot$ on 2017 September 6 at 12:24 UT. Then, the C3 coronagraph followed the CME up to a height of $4.99\,R_\odot$ at 12:30 UT. The height-time data profile indicated that the reported CME is a faster event with linear speed $1571\,\mathrm{km\,s^{-1}}$. A major X-class solar flare in solar cycle 24 erupted from geoeffective NOAA AR 2673 starting at 11:53 UT, ending at 12:10 UT and peaking at 12:02 UT on 2017 Sep 6. The event was the largest X-class flare reported during that day. It occurred just a few hours after a long-duration X2.2 at 09:33 UT. It is also the strongest solar flare from solar cycle 24. We used parameters of CMEs observed from *SOHO*/LASCO to calculate the CME arrival time from Sun to Earth. To calculate the arrival time of the CME from Sun to 1 AU, various parameters of CMEs along with solar wind conditions are necessary, besides various parameters associated with the actual CME-CME interaction during the IP space propagation (Mishra & Srivastava 2014; Shen et al. 2012; Temmer et al. 2012). In such interaction, a primary fast CME overtakes the next CMEs (one or more). To identify the possibility of CME-CME interaction in this case, we examine the CMEs that occurred just 2–3 days before on 2017 September 6 (12:24 UT). In Table 1, we list the CMEs observed during 2017 September 3–6. In Table 1; the second column gives the date and time of first detec-

tion of CME in the C2 coronagraph of LASCO. Position angle and angular width are denoted by PA and AW, respectively. LASCO observation shows that the speed of events occurred before.

2.3 Radio Dynamic Observations by Wind/WAVES

A dynamic spectrum of radio observations obtained from Wind/WAVES observed significant activities over a wide range of frequencies between 14 MHz which provide details and insights about the magnetic field and plasma processes driven by a flare/CME event in the solar surface and beyond. The signature of the initial magnetic field line opening can be inferred from type III radio bursts at the time of initiation and peak phase of first flare event (refer to Fig. 2 at $\sim$09:00 UT). As ascertained from Figure 5, the two type III radio bursts occurred around 12:00 UT which confirms the onset of the second flare and as the further opening of coronal magnetic fields. Type II emissions occur in association with eruptions on the Sun and typically indicate a CME is associated with a flare event. Here, the type II radio burst is observed at around 12:02 UT in the frequency range of 1–0.1 MHz in the Decameter-Hectometric (DH) spectrum displayed in Figure 5. The onset of type II radio burst and occurrence of type III radio burst provide the earliest indication of the CME initiation process. The duration and frequency range of this type II imply a height range of 6–25 $R_\odot$ with a speed of $\sim$1969 km s^{-1}. Also during this interval, strong patches of intensity enhanced emission in the type II radio burst is seen around 16:00–18:00 UT within the frequency range of 1–0.1 MHz. Do these intense patches reveal the interaction of a reported major CME with the previous CME at the height $\sim$5–10 $R_\odot$. The interaction signatures observed in the radio dynamic spectrum are consistent with the timings and locations of CMEs that occurred on 2017 September 6, as described in Section 3.2. Further, the comparisons of CME height-time plots obtained from LASCO indicate the possibilities of CME-CME interactions well beyond Wind/WAVES observing frequencies.

2.4 Observation Near Earth

In Table 2, we have listed the various IP parameters associated with the CME/Flare that occurred on 2017 September 6. We report the IP magnetic and plasma parameters of disturbances associated with the CME and the ambient solar wind observed near Earth in Figure 6. In Figure 6, from top to bottom, plots indicate variations of total magnetic field strength (nT), z-component of ambient solar wind magnetic field (nT), flow speed, proton density (n/CC), proton temperature (K), flow pressure and horizontal component of geomagnetic disturbance of the

Table 1 List of the CMEs Observed During 2017 September 3–6

| No	First C2 Appearance (UT)	Central PA (deg)	AW (deg)	Linear Speed (km s^{-1})	Accel (km s^{-2})
1	03Sep17 09:36	91	34	166	−7.9
2	04Sep17 00:48	191	29	288	29.7
3	04Sep17 07:00	356	5	188	−36.4
4	04Sep17 19:00	233	>205	597	52.9
5	04Sep17 20:12	halo	360	1418	47.5
6	05Sep17 15:42	261	47	377	2.5
7	05Sep17 17:36	216	129	474	6.4
8	06Sep17 07:12	256	64	113	6.8
9	06Sep17 09:48	245	80	391	−13.8
10	06Sep17 12:24	halo	360	1571	−0.3
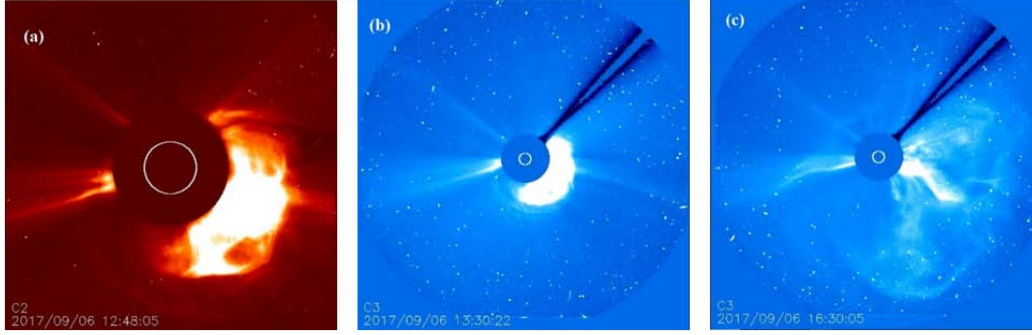
Fig. 3 Propagation difference image obtained from LASCO C2 (in panel (a)) and C3 (in panels (b)-(c)) demonstrating the propagation of the halo CME arising from NOAA AR 12673 on 2017 September 6.
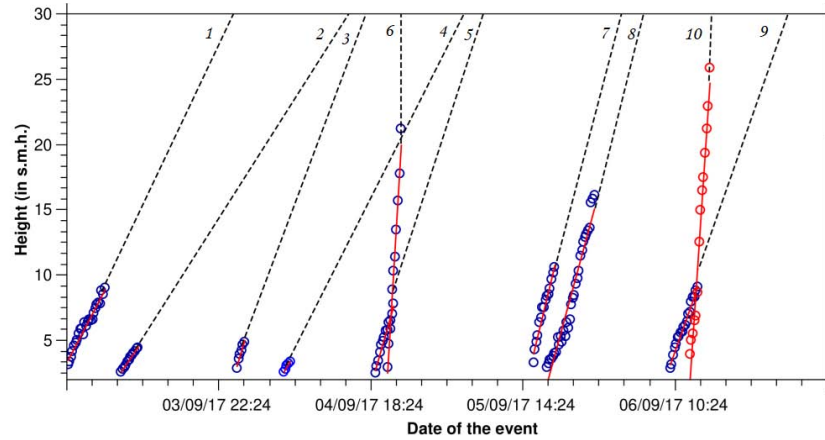
Fig. 4 Height-time profile of CMEs (marked 1–10) that occurred during 2017 September 3–6. The *dashed lines* indicate linear fittings to height-time data for the corresponding CMEs. In figure numbered 10 *blue circled plot* indicates the CME originated from NOAA AR 12673 on 2017 September 6.

field (high resolution Dst index) (nT). As one of the major IP disturbances, IP shocks link events that occurred at the Sun with moderate to extraordinary disturbances at the Earth, and greatly affect the near-Earth environment. When an IP shock collides with the Earth's magnetopause, great compression of the magnetosphere will cause a sudden impulse (SI) of the geomagnetic H-component at middle and low latitudes on the ground. Several aspects of geoeffectiveness related to IP shocks can be summarized as follows: (1) IP shocks are accompanied by large changes in solar wind dynamic pressure and thus significantly compress the Earth's magnetosphere, causing the SIs observed by ground-based magnetometers (Chao & Lepping 1974; Araki 1994); (2) IP shocks with southward interplanetary magnetic field (IMF) are important IP causes of geomagnetic storms (Tsurutani et al. 1988, 1992; Gonzalez et al. 1999; Echer et al. 2008b,a); (3) IP shocks can accelerate energetic particles during their propagation (Rao et al. 1967; Lee 1984; Desai et al. 2003) and trigger substorms (Tsurutani & Zhou 2003; Yamauchi et al. 2006;
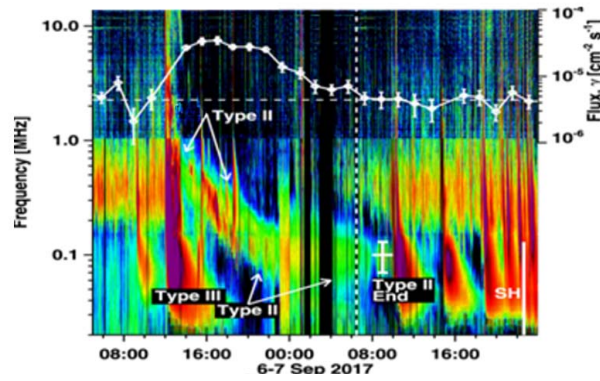
Fig. 5 Wind/WAVES type II burst starting around 14 MHz (~12:05 UT, 2017 September 6 and continuing down to ~100 kHz (09:00 UT, 2017 September 7. The end time is marked by the *short vertical line* with its length indicating the bandwidth (70–130 kHz). The *horizontal error bars* signify the end time uncertainty. The *vertical dashed line* marks the SGRE end (06:28 UT, September 7); the *horizontal dashed line* represents the gamma-ray background. The shock arrival time at 1 AU is labeled "SH".
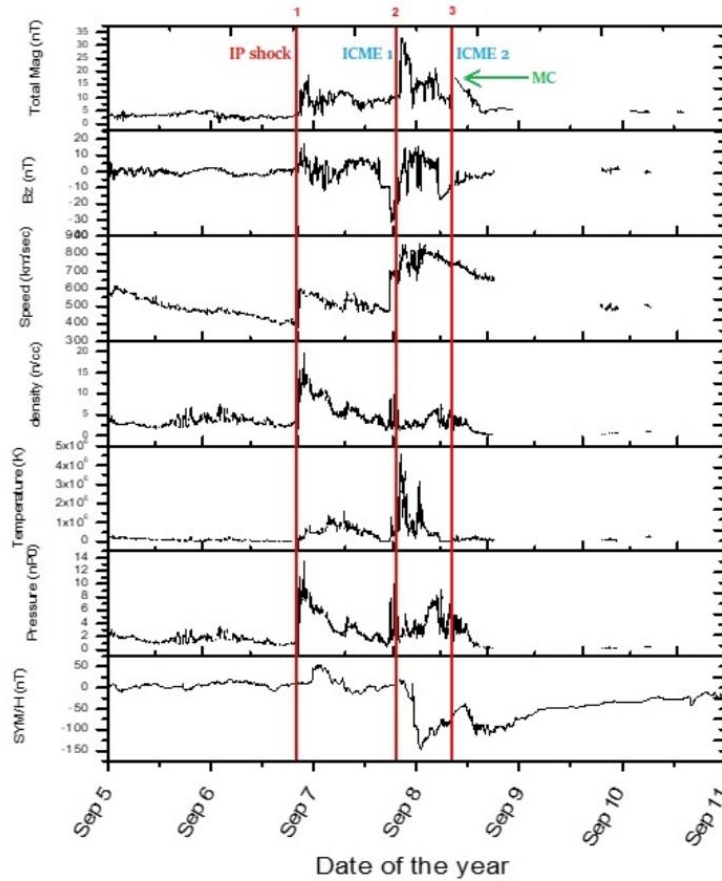
Fig. 6 The above plot shows the in-situ observations of magnetic field parameters and IP plasma during 2017 September 5–10. The plot indicates the variations of total magnetic field strength, z-component of the magnetic field, flow speed, proton density, proton temperature, flow pressure and SYM/H index from top to bottom respectively. The *first vertical red line* indicates arrival of the shock. The region between lines 2 and 3 represents the ICMEs recorded during that time. As per Richardson and Cane ICME catalogues from *http://www.srl.caltech.edu/ACE/ASC/DATA/level3/icmetable2.htm*, the start time of the first ICME is at 2017/09/07 20:00, and the second ICME arrived at 2017/09/08 11:00 which is signified by *red vertical line* 2 and 3 respectively.

Yue et al. 2010). Besides, most IP shocks observed within 1 AU can be identified with ICMEs. From Figure 6, we can see that the signature of shocked plasma at about 19:36 UT on 2017 September 7, highlighted by a vertical line (red) and indicated as (1), from in-situ measurements, exhibits large and sudden changes in most or all parameters of the magnetic field and plasma. The next fluctuations are evidence of ICMEs (numbered as (2) and (3) in

Table 2 In-situ Observations at 1 AU

Dst (Date Time VAlue)	ICME (Start Time and End Time)	Bz	MC	IP shock (Date Time)
08Sep17 02:00 –142	08Sep17 11:00 – 10Sep17 09:00	8	1	07Sep17 20:14

Fig. 6). The start time of the first ICME is at 2017/09/07 20:00, and the second ICME arrived at 2017/09/08 11:00 (*http://www.srl.caltech.edu/ACE/ASC/ DATA/level3/icmetable2.htm*), and it is believed that these two ICMEs are the signatures of geomagnetospheric disturbances corresponding with the two CMEs mentioned above. In Figure 6, we identify the magnetic cloud (MC) at 10:12 UT on 2017 Sep 8. An MC can be described as a particular type of IP ejection with the following characteristics at 1 AU, (a) relatively higher magnetic field strength compared to the background, (b) direction of magnetic field rotates with large and smooth angle during an interval of order of a day, and (3) relatively low proton count (Burlaga et al. 1981; Burlaga 1991; Burlaga et al. 2002, 1982; Osherovich & Burlaga 1997). We can also observe from Figure 6 that this major geomagnetic storm is caused by shock compression, which makes this geomagnetic storm so intense. The bottom plot of Figure 6 indicates the time evolution of the horizontal component of geomagnetic disturbance (i.e., SYM/H). From Figure 6, we can see a small fluctuation in the index, which is followed by the first shock at 18:45 UT on 2017 Sep 7. It starts decreasing followed by arrival of the second shock. The Dst index falls to a minimum value of –142 nT on 2017 Sep 8 at 02:00 UT and undergoes phase of recovery afterward.

2.4.1 Comparison with model predictions of arrival time of CME

Electromagnetic disturbances take only a few minutes to travel from the Sun to 1 AU, while solar wind takes a few days after originating from the Sun. CMEs are detected remotely by the white light coronagraph and also detected locally by spacecraft. Knowing the arrival time of a CME accurately is the most important aspect in predicting the space weather, because we know that, from various studies from the last two decades, most severe geomagnetic storms are caused by CMEs. In this work, we employed two CME prediction models to calculate the transit time of a CME or IP shock at 1 AU. We compile the CME actual arrival time that occurred on 2017 September 6 followed by the arrival time calculated by the Drag Based Model, i.e., DBM (Vršnak et al. 2013) and empirical shock arrival (ESA) model (Gopalswamy et al. 2001a). With the above models, to estimate the transit time of an ICME/IP shock, the necessary input parameters are based on measurements

of the CME by LASCO onboard *SOHO*, observed at locations near the Sun. Vrsnak et al., proposed DBM in 2013. According to DBM, the CME speed dragged due to ICME interaction of ambient solar wind. In DBM *http://oh. geof.unizg.hr/DBM/dbm.php*, the input parameters are: starting linear (radial) distance of CME (r0), speed of CME at r0 (v0), asymptotic solar wind and drag parameter. After inputting all the values for the CME that occurred on 2017 Sep 6 at 12:24 UT, we have arrived at the transit time of 39.49 h at 1 AU. The average speed of plasma flow recorded by the in-situ instrument is $450 \, \text{km s}^{-1}$, which we have taken as the asymptotic solar wind speed. The empirical CME arrival (ECA) model is built on the hypothesis that during the propagation of CMEs outward from the Sun, CMEs propagate with an effective constant acceleration and deceleration process. To calculate the transit time near Earth, we follow the Gopalswamy et al. (2001a) calculation method. Notably, the effective acceleration of a CME will stop at a distance d1 (cessation distance) before 1 AU, and it propagates the remaining distance d2 (d2 = 1 AU − d1) at a constant speed. The arrival time of a CME can be calculated by the formula t = t1 + t2, (where t1 is the time taken to travel up to acceleration cessation speed d1, and t2 is time to travel d2); (eqs. (6) and (7), Gopalswamy et al. 2001a). Syed Ibrahim et al. (2015) examine the transit period of major CMEs by ESA model for various acceleration cessation distances (0.5 AU, 0.6 AU and 0.7 AU) and they found the least error between actual and estimated transit time for a distance of 0.7 AU where acceleration cessation happens. So for our reported CME, the effective acceleration of CME from Sun to 0.7 AU (regarded as the acceleration cessation distance) is estimated as $-6.3 \, \text{m s}^{-2}$ (eq. (4), Gopalswamy et al. 2001a) and the arrival time for the CME is 33.56 h.

3 DISCUSSION AND CONCLUSIONS

In this work, we analyze the initiation, IP consequence and effect at 1 AU of an intense geoeffective CME associated with a major solar flare (X9.3 class) from the current solar cycle (solar cycle 24). The CME/flare occurred from NOAA AR 12673 located at S09W30 on the solar disk. The CME/flare originated from the complex magnetic configuration category alpha-beta-gamma. The multi-wavelength observations from SDO of the reported AR reveal a large system of coronal loops over the complex magnetic polarity regions on the surface of the Sun (photosphere) from an S-shaped, i.e., a coronal, sigmoid.

It was found from several studies that coronal sigmoid ARs are more eruptive than non-sigmoidal regions (Glover et al. 2000). It is also confirmed from many studies that the sigmoidal structure can be observed well in different EUV channels as well as in soft X-ray emission. The study of NOAA AR 12673 at 94 Å reveals the indication of intense emission from its core region due to the pre-existing large sigmoid. The initiation of eruption is from a complex magnetic bipolar region near the core that is subsequently associated with the sigmoid region. We regard these pre-flare observations as the confirmation of CME initiation. From the *GOES* profile, we can see the two successive flares, i.e. X2.2 class flare at 09:18 UT and X9.3 class flare at 12:02 UT, as temporal evolution of energy released during the process. Here, we studied the fast CME event that occurred on 2017 September 6 with a linear speed of $1571 \, \text{km s}^{-1}$, as displayed Figure 2. As this event is fast enough, it is very likely to interact with comparatively slow CMEs that occurred previously. In the dynamic DH radio spectrum (Fig. 5), the CME propagation is manifested as IP type II shock starting from 2017 September 6 at ~15:00 UT and continued up to 2017 September 7 at ~10:00 UT. The most interesting aspect of the type II emission is the occurrence of intense patches of enhanced brightness superimposed on the main type II structure. This kind of enhancement in radio emission during type II radio burst provides strong evidence for interaction of CMEs (Gopalswamy et al. 2001b; Manchester et al. 2017). Our analysis reveals CME-CME interaction from in-situ measurement. Complex interactions between CMEs are also ascertained at 1 AU. From Figure 6, we can see that a shock with low intensity precedes an extreme IP shock indicated as red (1 and 2) verticals lines. It seems that the first shock indicates the arrival of a low speed CME. The marker of the second major and high speed CME is associated with the second shock, which is followed by the onset of decline in Dst and dense sheath region. We can also observe from Figure 5 that this major geomagnetic storm is caused by shock compression. The observations near Earth clearly reveal two distinct MCs (separated by green dashed lines and marked as MC1 and MC2 in Fig. 6). It is suggested that these two MC structures evolved from overtaking or interactions from two successive CMEs. It is important to estimate the arrival time of solar eruption for predicting disturbances in the geomagnetic field. We can see that the ESA model calculation is closer than the DBM calculation to the actual shock arrival time. The distinct MCs (1 and 2) near Earth are the preserved signature of interacting CMEs, which are identified by abrupt variations in the magnetic field and plasma parameters, showing annihilation of magnetic flux. These multiple complex structure of varying intensities associated with ICMEs/IP shock contribute to the effectiveness of solar eruptions at 1 AU. From the observation near Sun, the IP medium and in-situ measurements at near Earth, we identify the process of interaction of CMEs from the source AR to the corona and IP space that have significant contribution to making this CME so geoeffective.

References

Amari, T., Luciani, J. F., Mikic, Z., & Linker, J. 2000, ApJ, 529, L49

Araki, T. 1994, Washington DC American Geophysical Union Geophysical Monograph Series, 81, 183

Brueckner, G. E., Howard, R. A., Koomen, M. J., et al. 1995, Solar Physics, 162, 357

Burlaga, L. F. E. 1991, Physics and Chemistry in Space, 21, 1

Burlaga, L., Sittler, E., Mariani, F., & Schwenn, R. 1981, J. Geophys. Res., 86, 6673

Burlaga, L. F., Klein, L., Sheeley, N. R., J., et al. 1982, Geophysical Research Letters, 9, 1317

Burlaga, L. F., Plunkett, S. P., & St. Cyr, O. C. 2002, Journal of Geophysical Research (Space Physics), 107, 1266

Canfield, R. C., Hudson, H. S., & McKenzie, D. E. 1999, Geophysical Research Letters, 26, 627

Chao, J. K., & Lepping, R. P. 1974, J. Geophys. Res., 79, 1799

Desai, M. I., Mason, G. M., Dwyer, J. R., et al. 2003, ApJ, 588, 1149

Echer, E., Gonzalez, W. D., & Tsurutani, B. T. 2008b, Geophys. Res. Lett., 35, L06S03

Echer, E., Gonzalez, W. D., Tsurutani, B. T., & Gonzalez, A. L. C. 2008a, Journal of Geophysical Research (Space Physics), 113, A05221

Glover, A., Ranns, N. D. R., Harra, L. K., & Culhane, J. L. 2000, Geophysical Research Letters, 27, 2161

Gonzalez, W. D., Tsurutani, B. T., & Clúa de Gonzalez, A. L. 1999, Space Science Reviews, 88, 529

Gopalswamy, N., Lara, A., Yashiro, S., Kaiser, M. L., & Howard, R. A. 2001a, J. Geophys. Res., 106, 29207

Gopalswamy, N., Yashiro, S., Kaiser, M. L., Howard, R. A., & Bougeret, J.-L. 2001b, ApJ, 548, L91

Gopalswamy, N., Lara, A., Manoharan, P. K., & Howard, R. A. 2005, Advances in Space Research, 36, 2289

Gopalswamy, N., Yashiro, S., Michalek, G., et al. 2009, Earth Moon and Planets, 104, 295

Gosling, J. T., Pizzo, V., & Bame, S. J. 1973, J. Geophys. Res., 78, 2001

Inoue, S., Shiota, D., Bamba, Y., & Park, S.-H. 2018, The Astrophysical Journal, 867, 83

Jiang, C., Zou, P., Feng, X., et al. 2018, ApJ, 869, 13

Joshi, B., Ibrahim, M. S., Shanmugaraju, A., & Chakrabarty, D. 2018, Solar Physics, 293, 107

Lee, M. A. 1984, Advances in Space Research, 4, 295

Lin, J., & Forbes, T. G. 2000, Journal of Geophysical Research, 105, 2375

Lugaz, N., Farrugia, C. J., Davies, J. A., et al. 2012, ApJ, 759, 68

Manchester, W., Kilpua, E. K. J., Liu, Y. D., et al. 2017, Space Science Reviews, 212, 1159

Manoharan, P. K. 2006, Solar Physics, 235, 345

Mishra, W., & Srivastava, N. 2014, ApJ, 794, 64

Mitra, P. K., Joshi, B., Prasad, A., Veronig, A. M., & Bhattacharyya, R. 2018, ApJ, 869, 69

Osherovich, V., & Burlaga, L. F. 1997, Washington DC American Geophysical Union Geophysical Monograph Series, 99, 157

Rao, U. R., McCracken, K. G., & Bukata, R. P. 1967, J. Geophys. Res., 72, 4325

Richardson, I. G., & Cane, H. V. 2010, Sol. Phys., 264, 189

Shen, C., Wang, Y., Wang, S., et al. 2012, Nature Physics, 8, 923

Shen, C., Chi, Y., Wang, Y., Xu, M., & Wang, S. 2017, Journal of Geophysical Research (Space Physics), 122, 5931

Shen, C., Xu, M., Wang, Y., Chi, Y., & Luo, B. 2018, ApJ, 861, 28

Shibata, K. 1999, Astrophysics and Space Science, 264, 129

Syed Ibrahim, M., Shanmugaraju, A., & Bendict Lawrance, M. 2015, Advances in Space Research, 55, 407

Temmer, M., Vršnak, B., Rollett, T., et al. 2012, ApJ, 749, 57

Tsurutani, B. T., Gonzalez, W. D., Tang, F., Akasofu, S. I., & Smith, E. J. 1988, J. Geophys. Res., 93, 8519

Tsurutani, B. T., Gonzalez, W. D., Tang, F., & Lee, Y. T. 1992, Geophys. Res. Lett., 19, 73

Tsurutani, B. T., & Zhou, X. Y. 2003, Advances in Space Research, 31, 1063

Vršnak, B., Žic, T., Vrbanec, D., et al. 2013, Solar Physics, 285, 295

Yamauchi, M., Iyemori, T., Frey, H., & Henderson, M. 2006, Journal of Geophysical Research (Space Physics), 111, A04217

Yan, X. L., Wang, J. C., Pan, G. M., et al. 2018a, ApJ, 856, 79

Yan, X. L., Yang, L. H., Xue, Z. K., et al. 2018b, ApJ, 853, L18

Yang, S., Zhang, J., Zhu, X., & Song, Q. 2017, The Astrophysical Journal, 849, L21

Yue, C., Zong, Q. G., Zhang, H., et al. 2010, Journal of Geophysical Research (Space Physics), 115, A00I05